Thickness-driven first-order phase transitions in manganite ultrathin films

Hongyan Chen,[1,*] Yang Yu,[1] Zhe Wang,[1,*] Yu Bai,[1] Hanxuan Lin,[1] Xiaolong Li,[6] Hao Liu,[1] Tian Miao,[1] Yunfang Kou,[1] Yongsheng Zhang,[3] Yan Li,[3] Jin Tang,[3] Zechao Wang,[5] Peng Cai,[1,2] Yinyan Zhu,[1] Zhaohua Cheng,[3] Xiaoyan Zhong,[5] Wenbin Wang,[1,2,4] Xingyu Gao,[6] Lifeng Yin,[1,2,4,†] Ruqian Wu,[1,2,‡] and Jian Shen[1,2,4,§]

[1]*State Key Laboratory of Surface Physics and Department of Physics, Fudan University, Shanghai 200433, China*

[2]*Institute for Nanoelectronics Devices and Quantum Computing, Fudan University, Shanghai 200433, China*

[3]*Beijing National Laboratory for Condensed Matter Physics, Chinese Academy of Sciences, Beijing 100190, China*

[4]*Collaborative Innovation Center of Advanced Microstructures, Nanjing University, Nanjing 210093, China*

[5]*National Center for Electron Microscopy in Beijing, Key Laboratory of Advanced Materials (MOE), The State Key Laboratory of New Ceramics and Fine Processing, School of Materials Science and Engineering, Tsinghua University, Beijing 100084, People's Republic of China*

[6]*Shanghai Institute of Applied Physics, Chinese Academy of Sciences, Shanghai 201204, China*

(Received 29 January 2018; revised manuscript received 30 May 2019; published 12 June 2019)

We report thickness dependent inhomogeneous antiferromagnetic (AFM) to ferromagnetic (FM) phase transitions in ultrathin $La_{0.7}Sr_{0.3}MnO_3$ (LSMO) films grown on the $SrTiO_3$ substrate. When the films are 4–7 unit cells (UCs) thick, FM domains appear as isolated nanodisks in the AFM matrix that together floats on top of the three AFM base UCs, leading a superparamagnetic blocking behavior. Our first principles calculations unravel the rather counterintuitive physical origin of this mixed phase state; the formation of FM/AFM domain boundaries is energetically favorable. At 8 UCs, an abrupt shear strain relief occurs in the LSMO thin film and twinning patterns with two unit cell periodicity form along the [010] and [100] directions. Our studies reveal the complexity of the magnetic phase transition at the nanometer scale and open a door for the development of quantum devices and statistical theories.

DOI: 10.1103/PhysRevB.99.214419

I. INTRODUCTION

The evolvement of phase domains during the phase transition of complex materials is of core importance for the design of innovative nanodevices as well as for the advance of fundamental science [1–3]. In this realm, ultrathin magnetic oxide films have been widely used as prototypes because of their rich electronic and magnetic phases and the strong interplay between lattice strain, electron correlation, and magnetic ordering in the two-dimensional (2D) limit. Among these materials, perovskite manganites such as $La_{1-x}Sr_xMnO_3$ (LSMO) have attracted the most interest ever since the discovery of their extraordinary properties such as the colossal magnetoresistance [4] and half-metallicity [5], very promising for applications in spintronic devices [6–12]. While the bulk LSMO has a uniform ferromagnetic (FM) metallic state without spatial electronic inhomogeneity or magnetic phase separation, LSMO films may exhibit dramatically different physical properties especially in the ultrathin regime [13–18]. For example, it was reported that LSMO ultrathin films grown on $SrTiO_3$(001) (STO) substrates exhibited complex magnetic and transport behaviors with multiple thickness-driven phase transitions [14,16,19,20]. At or below 3 unit cells (UCs), LSMO films are observed to be insulating with a C-type antiferromagnetic (AFM) configuration [13,18,21]. In the thickness range between 4 and 7 UCs, LSMO films remain insulating [13,16,19,21] but show a low net magnetization [13,14,16]. Above 8 UCs, LSMO films recover the bulk-like high spin FM state [13]. Such rapid changes of spin and electronic states in a single material system provide an ideal case for studies of critical behaviors of complex 2D magnetic films.

In this letter, we aim at unraveling the driving forces for the thickness-dependent AFM to FM phase transition in LSMO ultrathin films grown on STO substrates. Using a suite of characterization tools including scanning tunneling microscopy (STM), transmission electronic microscopy (TEM), synchrotron-based surface X-ray diffraction (XRD), and time-dependent magneto-optical Kerr effect (MOKE), we examined the structural and magnetic phase changes in LSMO/STO thickness wedge samples. Strikingly, a different inhomogeneous magnetic phase is found when LSMO films are 4–7 UCs thick. While the bottom 3 UCs remain in their C-type AFM state, the top 1–4 UCs contain FM nanodisks in the AFM matrix, making the film inhomogeneous in both lateral and vertical directions. Our first principles calculations revealed that the appearance of this unusual phase stems from a counterintuitive circumstance: the formation of FM/AFM domain boundaries releases rather than costs energy due to the interplay between the charge state of Mn ions, strain, and magnetic ordering. This calls for attention to the crucial role of phase domain boundaries for phase transitions in complex nanosystems, where the conventional statistical theory breaks

[*]These authors contributed equally to the work.

[†]Authors to whom correspondence should be addressed: lifengyin@fudan.edu.cn

[‡]wur@fudan.edu.cn

[§]shenj5494@fudan.edu.cn

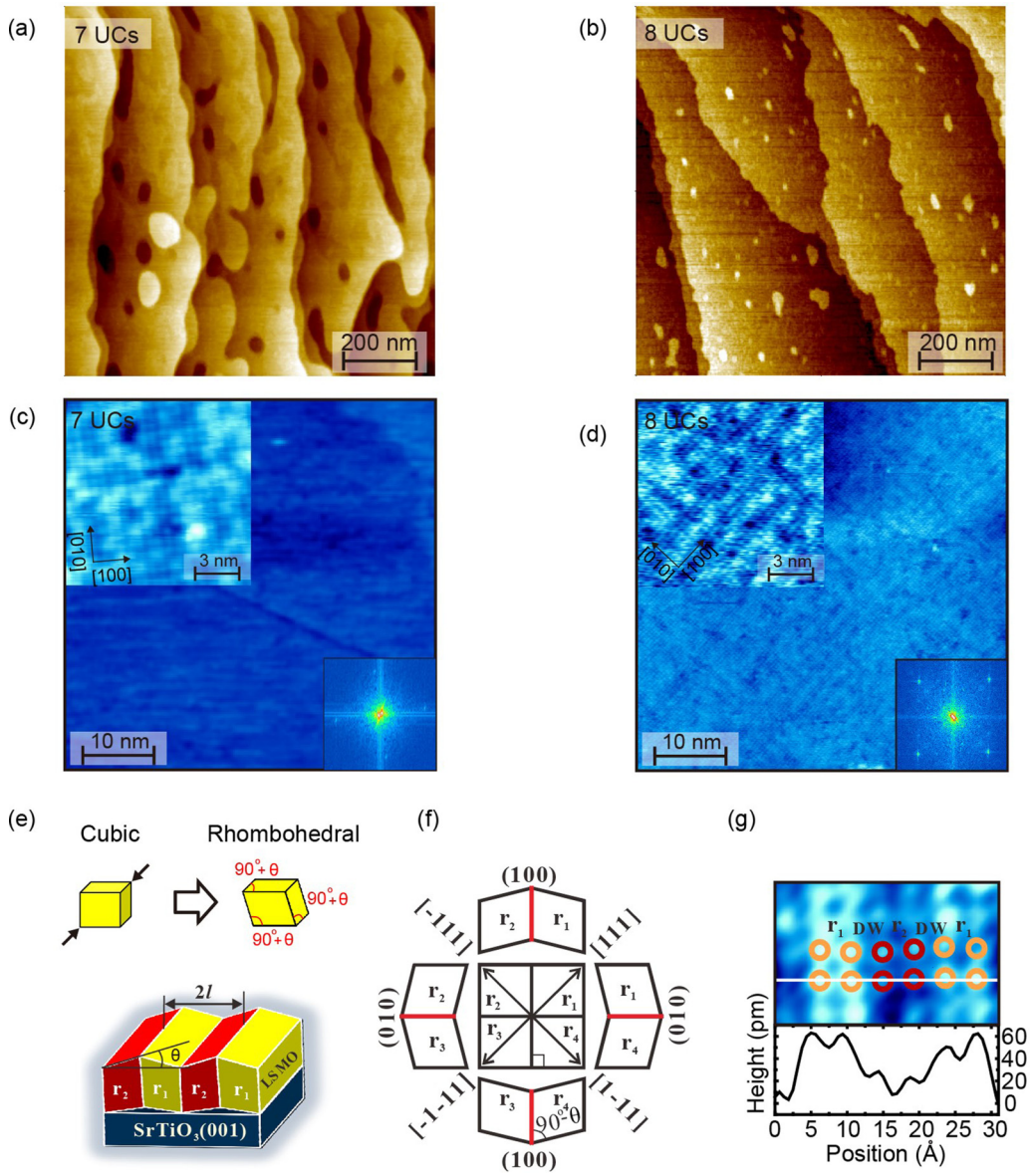

FIG. 1. STM images and structural properties of LSMO ultrathin films. (a) and (b) are 1 um × 1 um large scale STM images of 7- and 8-UC LSMO films, respectively. (c) and (d) are 50 nm × 50 nm STM image of 7- and 8-UC LSMO films, respectively. The insets are zoom-in images with atomic resolution, which show clearly a 1 × 1 lattice for the 7-UC film and a periodic pattern with two atomic lattice spacing for the 8-UC film. The FFT of the STM images are also shown as additional insets in the bottom. (e) Schematics of cubic to rhombohedral structural transition and the nanotwinning patterns of the LSMO ultrathin film grown on STO substrate. (f) Schematics of four rhombohedral domain pairs of nanotwinning in the projection of (001) plane, i.e., (100)-r_1/r_2, (010)-r_2/r_3, (100)-r_3/r_4, and (010)-r_4/r_1. (g) High-resolution STM image and corresponding line profile of the 8-UC film indicate that the lattice has a small distortion angle compared to the cubic unit cell along both out-of-plane and in-plane directions. Our STM experiments were performed with $V_{\text{bias}} = 2.0$ V and $I = 30$ pA.

down. Moreover, the possibility of creating and manipulating nonuniform magnetic structures may find important uses in technological innovations.

II. EXPERIMENTAL DETAILS

Epitaxial $La_{1-x}Sr_xMnO_3$ ($x = 0.3$) films were grown on 0.5% Nb-doped STO (001) [or undoped STO (001) for transport measurements] substrates using pulse laser deposition (PLD) (248 nm, 2 Hz, 1 J/cm^2 fluence) in a multichamber ultrahigh vacuum system equipped with STM (base pressure $<1 \times 10^{-10}$ Torr). Prior to growth, the substrates were chemically etched by buffered HF, followed by preannealing at 950 °C in an adequate flowing O_2 environment to form an atomically flat Ti-O_2 terminated surface [22]. During growth, the substrate was held at 820 °C in an oxygen (8% ozone) environment of 3×10^{-2} Torr. The thickness of the films was monitored by unit cell intensity oscillations of reflection high-energy electron diffraction (RHEED). As shown in Figs. 1(a) and 1(b), a flat sample surface with clear atomic steps inherited from the substrate can be obtained, which indicates a good epitaxial thin film growth. The thickness wedge sample of LSMO films were fabricated by adding a mask in front of the growing sample. By carefully controlling the shielded area,

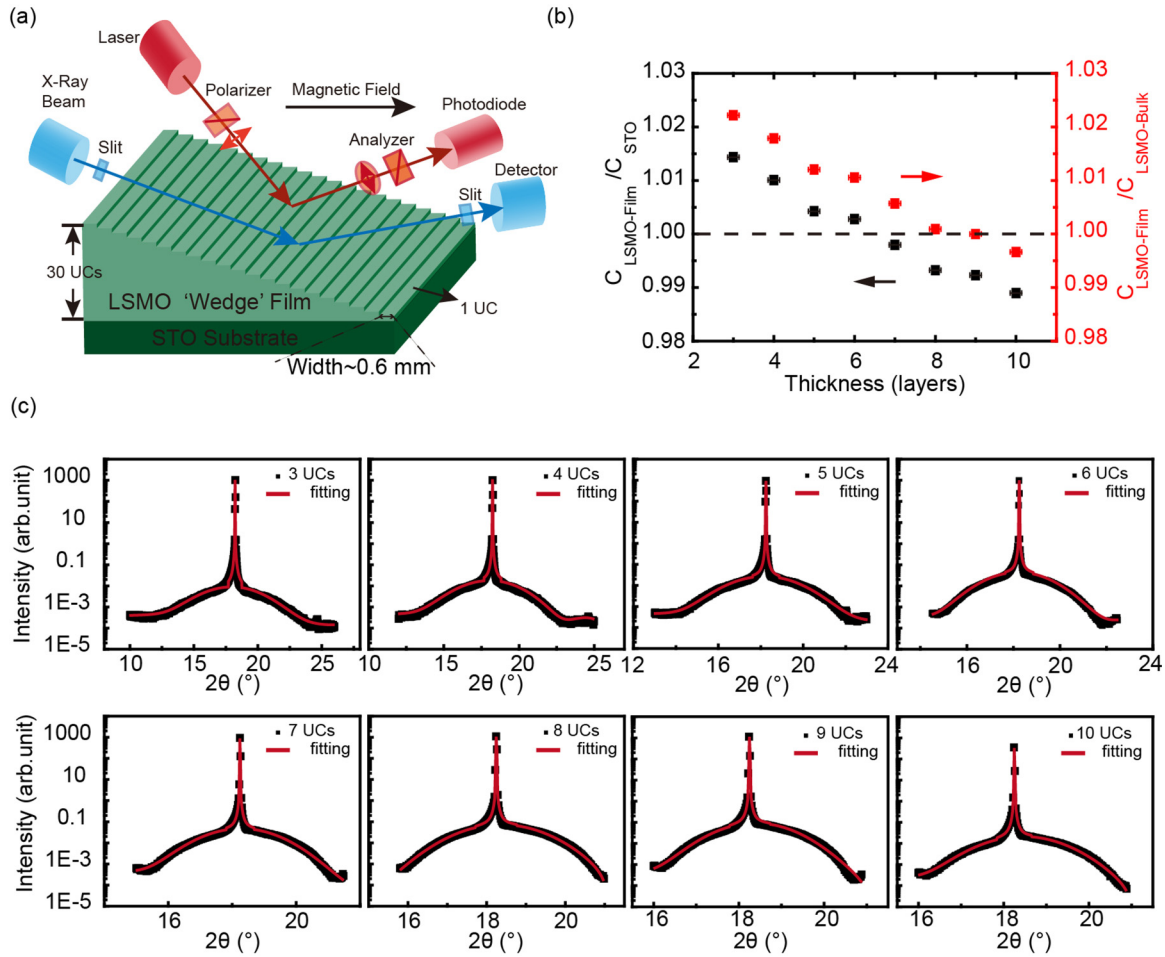

FIG. 2. XRD measurements of a LSMO wedge sample. (a) Schematics of XRD (and MOKE) measurements on LSMO thickness wedge sample. (b) Out-of-plane lattice parameters (c) of the films with different thicknesses, compared with that of STO substrate and bulk LSMO. (c) Typical x-ray diffraction patterns of LSMO ultrathin films grown on STO substrate with thickness ranging from 3 to 10 UCs, respectively. The black dots represent the experimental XRD data, and the red lines are the fitting curves. The fitting of XRD patterns are using program MAUD.

the thicknesses of the wedge can be designed to increase layer by layer with the width of the layer step about 0.6 mm. The schematic of thickness wedge sample was shown in Fig. 2(a). More details can be found in Appendix A.

Up to 7 UCs, the rhombohedral LSMO thin films are fully strained on the cubic STO substrates with atomically flat surfaces, as shown in Fig. 1(c). Strikingly, by increasing the thickness to 8 UCs, dramatic changes occur in the films with the appearance of protruded atomic rows along the orthogonal [010] and [100] directions [Fig. 1(d)]. The insets show the magnified atomically resolved images and the corresponding fast Fourier transform (FFT) images, revealing a normal "1 × 1" and a rarely seen "4 × 1" structures, respectively. A detailed analysis reveals that the 4 × 1 superstructures represent twinning domains with a periodicity of two atomic lattice spacing caused by relief of shear strain between the rhombohedral LSMO thin films and the cubic STO substrates [23–27].

To understand the nature, one may view the rhombohedral structure of the LSMO as a compressed cubic unit cell along the ⟨111⟩ direction, as shown in Fig. 1(e) (top panel). The schematics (bottom panel) exhibit the nanotwinning patterns of LSMO ultrathin films grown on a STO substrate after transition from a cubic to a rhombohedral structure. As sketched, the neighboring twinning domains will have a small angle (θ) sheared both in the plane and out-of-plane. In the cubic unit cell, the four ⟨111⟩ directions are equivalent, giving rise to four rhombohedral domain pairs when projecting to the (001) plane, which are (100)-r_1/r_2, (010)-r_2/r_3, (100)-r_3/r_4, and (010)-r_4/r_1 [Fig. 1(f)] [28]. The high-resolution image in Fig. 1(g) shows that the film consists of two alternating domains with the unit cells compressed in the [111] and [−111] directions, respectively. This is a typical (100)-r_1/r_2 domain pair with the high (marked by orange circles) and low valleys (marked by red circles). Combining with the corresponding line profile, Fig. 1(g) shows that the lattice in the twinning domains has a small angle distortion compared to the cubic unit cell in both out-of-plane and in-plane directions, which closely resemble the rhombohedral-like crystal structure. Quantitatively, as sketched in Fig. 1(e), the shear strain relaxation induced an out-of-plane tilting angle and the domain width can be denoted as θ and l, respectively. Therefore, from the Fig. 1(g), we obtain the height difference (Δh) of two twinning stripes to be about 0.3 Å. For the fully

TABLE I. Out-of-plane lattice parameters (c) of the films with different thicknesses and the corresponding errors obtained based on the fitting. The fitting results of STO substrate are also shown here as a comparison.

	Thickness (layers)	Lattice Constants (Å)	Errors (Å)		Lattice Constants (Å)	Errors (Å)
LSMO	3	3.961	0.004737	STO	3.905	1.42×10^{-4}
	4	3.944	0.004228		3.905	1.39×10^{-4}
	5	3.921	0.003822		3.905	1.25×10^{-4}
	6	3.915	0.003004		3.905	1.39×10^{-4}
	7	3.897	0.003082		3.905	1.02×10^{-4}
	8	3.878	0.002240		3.905	9.73×10^{-5}
	9	3.874	0.002440		3.905	1.16×10^{-4}
	10	3.861	0.002022		3.905	6.73×10^{-5}

strained LSMO on STO, the in-plane lattice constants are $a = b = 3.905$ Å. The estimated θ is thus arctan $(\Delta h/l) \sim 2.7°$, which is about ten times larger than that of the bulk $La_{0.7}Sr_{0.3}MnO_3$ (∼0.268°) [11].

Figure 2 shows the thickness-dependent change of lattice constant along the perpendicular c axis obtained by surface XRD measurements from the thickness wedge sample of LSMO/STO. The schematics of XRD measurements are shown in Fig. 2(a). The beam size at the sample is approximately $0.2 \times 0.2\,mm^2$ and is confined by vertical and horizontal slits. So the x-ray beam can be well performed on the wedge sample with a terrace width (∼0.6 mm) for each thickness larger than the beam size. The XRD patterns of the LSMO thickness wedge on the STO substrate are shown in Fig. 2(c). The profiles are analyzed using the Material Analysis Using Diffraction (MAUD) program [29]. The lattice constants and the errors are obtained based on the fitting shown in Table I. The fitted out-of-plane lattice constant of the STO substrate has a negligible error bar implies that the fitting is reliable. [A description of the error bars in Fig. 2(b) is presented in Appendix B].The refined c-axis lattice parameter of the LSMO ultrathin films are shown in Fig. 2(b), plotted as a function of thickness by comparing with the c-axis lattice parameter of the STO substrate (out-of-plane lattice constant = 3.905 Å) and the bulk LSMO (out-of-plane lattice constant = 3.875 Å). Unexpectedly, the c-axis lattice constant of the tensile strained LSMO film remains to be larger than that of the LSMO bulk up to 7 UCs on STO. Above 8 UCs, the c-axis lattice constant becomes smaller than that of the bulk LSMO, normal for a tensile strained film. Interestingly, this occurs at the same critical thickness when the films' shear strain is relieved.

The shear strain relief appears to have dramatic influence on the magnetic properties of the sample. We apply a magnetic field along the in-plane easy magnetization axis, i.e., the [110] direction (see Appendix C) and measure hysteresis curves of 3–9-UC-thick films at 10 K. At 3 UCs or below, no net magnetization can be detected as shown in Fig. 3(a). Above 3 UCs, the magnetization increases with thickness and jump to a large value at 9 UCs. This is more obvious in Fig. 3(b), which depicts the thickness dependence of the saturation magnetization. Because all data are collected from the same sample in the same condition, the thickness dependence of the magnetization can be reliably used to deduce the evolution of magnetic state. Apparently, the magnetic behavior of LSMO films can be divided into four regions. In region I (1–3 UCs), the films are in an AFM state with the C-type spin configuration [18]. In region II (4–7 UCs), the magnetization increases linearly with the thickness and the slope extrapolates back to zero at 3 UCs, indicating that the 3 base UCs remain to be AFM even in region II. The magnetization of the 8-UC film (region III) starts to visibly deviate from the trend in region II. In region IV (9 UCs and above), the magnetization again increases linearly with thickness but the slope is about

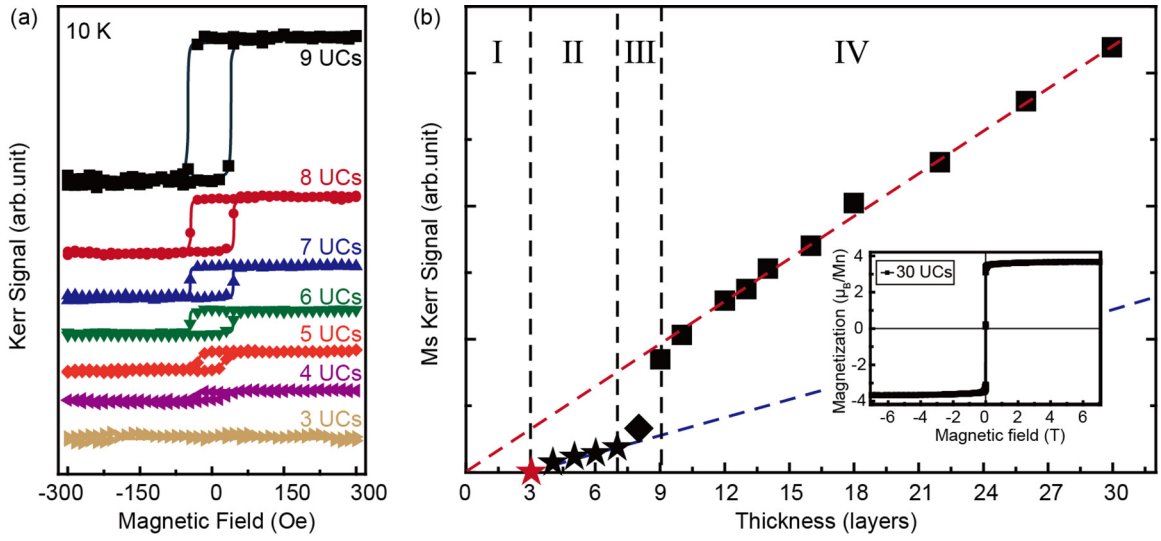

FIG. 3. Magnetic properties of LSMO ultrathin films. (a) MOKE hysteresis loops measured at 10 K, from 3 to 9 UCs. The ferromagnetic signal disappears at 3 UCs. (b) Saturation magnetization as a function of film thickness measured at 10 K, from 3 to 30 UCs. The red and blue dash line are fitting curves of 9–30 UCs and 4–7 UCs signals, respectively. The red line back extrapolates to zero, while the blue line intercepts thickness axis at 3 UCs. The inset is the magnetic hysteresis loop of a 30-UC thick LSMO film measured at 10 K by SQUID. The magnetic field applied in the easy axis, i.e., [110] direction, and it shows the saturation moment of 3.6 μ_B/Mn.

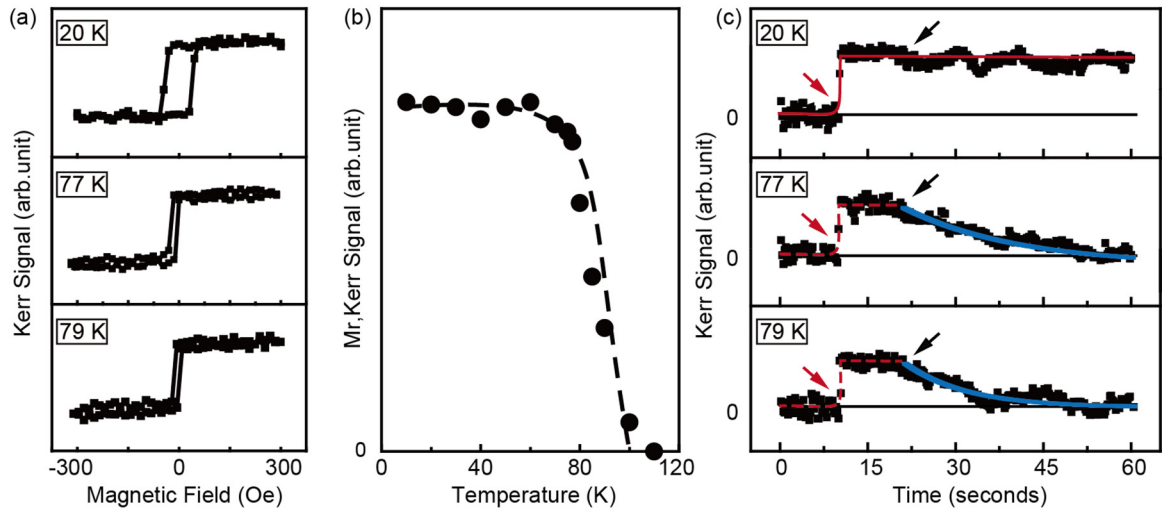

FIG. 4. Superparamagnetic behavior of the 6-UC LSMO film. (a) MOKE hysteresis loops measured at 20, 77, and 79 K. (b) M_r vs temperature of the film. (c) Time dependence of the magnetization of the 6-UC film measured at 20, 77, and 79 K. An in-plane external field was switched on (off) at the time points indicated by the red (black) arrows. The red lines are guides for the eyes. The blue solid lines are the fitting curves plotted according to Eq. (2) by applying the relaxation time (τ) of 19.5 and 10.5 s for 77 and 79 K, respectively (see Appendix E).

two times larger than that in region II. Moreover, the linear slope extrapolates back to zero at the origin, indicating that entire film, including the 3 base UCs, becomes uniformly ferromagnetic. The magnetic moment in region IV is 3.6 μ_B/Mn, according to superconducting quantum interference device (SQUID) measurements for a 30-UC film [inset of Fig. 3(b)]. From the slopes, we can deduce the averaged local moment of the magnetic part in region II, i.e., the additional layers above the 3 base UCs, is ∼1.8 μ_B/Mn. This is considerably smaller than the moment of Mn ions in typical ferromagnetic manganites [13].

The low magnetic moment in region II may be attributed to two possible causes: (1) the layers are in a canted AFM state; (2) the layers are in a mixed phase state, with FM metallic islands embedded in the AFM insulating regions, because the films are known to be insulating below 8 UCs [13,16,19] (see Appendix D, Fig. 11). The major difference between these two cases is that the mixed phase state lacks long-range order and hence the sample should exhibit a superparamagnetic behavior near or above the blocking temperature. A distinct feature of such superparamagnetic behavior is that the remanent magnetization (M_r) decays with time, whereas M_r of the canted AFM state is stable. Therefore, we performed time-dependent MOKE measurements in the 6-UC region of the thickness wedge. As shown in Fig. 4, the film exhibits a FM-like behavior with magnetic hysteresis loops [Fig. 4(a)]. Even the temperature dependence of M_r resembles that of a FM system, with a critical temperature of ∼100 K [Fig. 4(b)]. However, when M_r is measured with time, it becomes clearly different from that of systems with a long-range magnetic ordering. For the time-dependent MOKE measurements, the film was first set in a demagnetized state as shown in Fig. 4(c) (zero Kerr signal indicated by the horizontal solid line). An external magnetic field (300 Oe) was then applied along the easy axis, leading to a sudden increase of the Kerr signal. The magnetic field is then switched off, and the evolution of M_r with time is recorded. Although M_r is relatively stable at low temperatures (20 K), it clearly decays with time at 77 and 79 K, which are still well below the "critical temperature" as displayed in Fig. 4(b). It is thus clear that the three additional UCs in the 6-UC film is superparamagnetic without true long-range order. The peculiar magnetic phase of LSMO films in region II is sketched in Fig. 5(a); the top layers have isolated FM disks in the AFM matrix, while the bottom 3 UCs are in AFM state. This special region is highlighted by two dashed lines in Fig. 5(b).

The size of the isolated FM disks can be estimated using the Néel-Arrhenius equation $\tau = \tau_0 \exp(\frac{KV}{k_B T})$ [30]. To determine the effective anisotropy constant, K, we measured the initial magnetization curves of the 6-UC film along the out-of-plane [001] direction and three in-plane main crystallographic directions, [110], [100], and [−110]. Apparently, the [001] direction is the hardest direction, while the second hardest axis is along the [100] direction [Fig. 6]. It is thus reasonable to assume that the magnetic relaxation passes through the in-plane anisotropy barrier, which can be estimated from the saturation field along the in-plane [100] hard axis (∼2000 Oe). The measured decay times τ are 19.5 and 10.5 s at 77 and 79 K, respectively [Fig. 4(c)]. A simple calculation yields the attempt time, $\tau_0 \sim 4.6 \times 10^{-10}$ s, quite reasonable for ferromagnetic systems [31]. The estimated volume of the FM disks in the film is ∼13000 nm^3, corresponding to 120 nm in diameter (more details about the calculations can be found in Appendix E).

III. FIRST PRINCIPLES CALCULATIONS AND DISCUSSION

We perceived that the formation of such an unusual magnetic configuration in LSMO films is due to the competition of several energy terms. Using the sketch in Fig. 5(a), R and h (in units of UC) as the radius and height of the FM disks, the total energy of the AFM film with one disk in a volume (V)

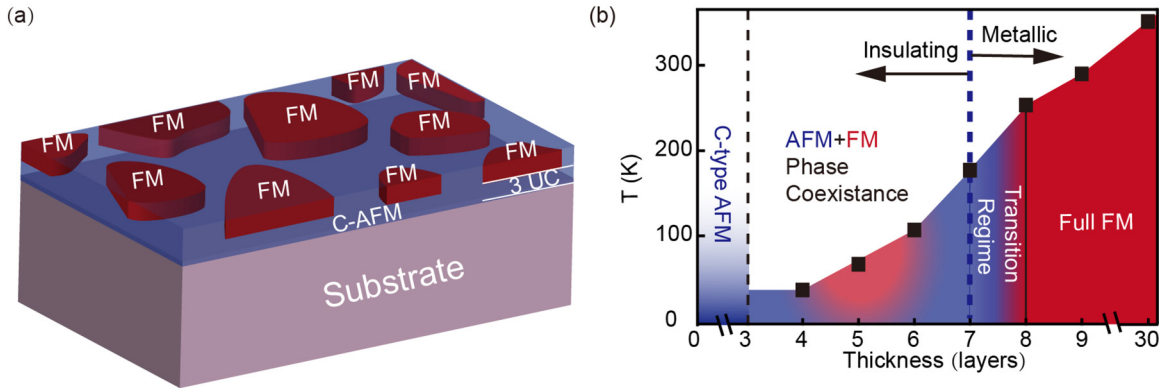

FIG. 5. (a) Schematic of the unusual spin structure of 4–7-UC-thick LSMO films. (b) Phase diagram of LSMO films from the ultrathin regime to the thick area.

can be expressed as

$$E = h\pi R^2 \cdot E_{\mathrm{FM}} + (V - h\pi R^2) \cdot E_{\mathrm{AFM}} + \pi R^2 \cdot E^{\perp}_{\mathrm{Form}} + 2h\pi R \cdot E^{\parallel}_{Form,}$$

where E_{FM} and E_{AFM} are the energies of bulk FM and AFM per unit cell volume, $E^{\parallel}_{\mathrm{Form}}$ and $E^{\perp}_{\mathrm{Form}}$ are the in-plane and out-of-plane formation energies per unit cell area, respectively. By applying the relations of $E_{\mathrm{AFM}} - E_{\mathrm{FM}} = 32J_{\parallel}$, $E^{\perp}_{\mathrm{Form}} \approx 8J_{\perp} > 0$, where $J_{\parallel}$ and $J_{\perp}$ are the in-plane and out-of-plane exchange interaction parameters, we can see that the mixed phase in indeed more favorable under following conditions: $E^{\parallel}_{\mathrm{Form}} < 0$ and $J_{\parallel}/J_{\perp} < 1/(4h)$. Note that for $E^{\parallel}_{\mathrm{Form}}$ the contribution of the exchange interaction term is zero at the FM and C-type AFM interface, and it is rather unusual to find a magnetic material with negative $E^{\parallel}_{\mathrm{Form}}$. The phase diagram in the parameter space ($E^{\parallel}_{\mathrm{Form}}$, $J_{\parallel}/J_{\perp}$) is shown in Fig. 7(a).

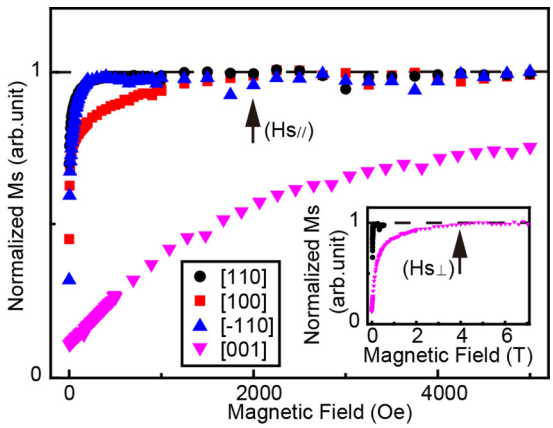

FIG. 6. Normalized initial magnetization curves along different directions of 6-UC LSMO thin film grown on STO (001) measured at 77 K. The arrow marks the in-plane saturation magnetic field ($\mathrm{Hs}_{\parallel}$), at which the film reaches the saturated magnetization (M_s) at different directions. The inset shows the normalized initial magnetization curves along the in-plane easy axis [110] and the hard axis [001] along the surface normal direction of the thin film, which shows a much larger saturation field in the out-of-plane direction (marked by black arrow).

Quantitatively, we performed density functional theory (DFT) calculations for various LSMO structures, using the Vienna *ab initio* simulation package (VASP) [32,33] with the projector augmented wave method [34,35] and generalized-gradient approximation in the Perdew, Berke, and Ernzerhof [36] format. The localized $3d$ states of Mn atoms were treated by effective on-site electron-electron correlation $U - J = 3\,\mathrm{eV}$. The $4\sim7$-UC LSMO films were simulated by the "strained bulk" approach, in which the substrate effect, including the epitaxial tensile strain (0.39%) and symmetry constraint (tilt of the MnO_6 octahedron about a/b axis is restricted), were taken into account by adopting an $I4/mcm$ space group unit cell with the in-plane lattice constants fixed to $a = b = 1.0039\,a_0$ ($a_0 = 7.85\,\text{Å}$ is the theoretical lattice constant of $R\bar{3}c$ rhombohedra LSMO). The out-of-plane lattice was varied from $c/a = 1.00$ to 1.02 to match the experimental values of different thickness. Two out of eight La atoms were substituted by Sr in the 40-atom unit cell to simulate the doping level, and all the atomic coordinates were fully relaxed. The spin structure of the AFM LSMO area is assumed to be C-type, which nonetheless shows a rich charge/orbital ordering (COO) phase. While the FM LSMO is a stable semimetal with itinerate e_g electrons around the Fermi level, we found two types of C-AFM states for bulk LSMO. One is the insulating (referred to as AFM-I) and has an alternating changes of Mn-O-Mn bond lengths along the modulation vector $\mathbf{q} = (0.5, 0.5)$. The other is the metallic (referred to as AFM II) and has an energy 46 meV higher than AFM-I, and the alternating change of Mn-O-Mn bonds is along the modulation vector $\mathbf{q} = (0.5, 0.0)$.

Using a 200-atom supercell along the [100] direction to model the in-plane interface, with five C-AFM and five FM $Mn\text{-}O_2$ planes as shown in Fig. 7(b), the formation energy of the interface is calculated by

$$E^{\parallel}_{\mathrm{Form}} = \tfrac{1}{2}(E_{\mathrm{total}} - E_{\mathrm{AFM}} - E_{\mathrm{FM}}),$$

where E_{total} is the total energy of the AFM/FM supercell, and E_{AFM} and E_{FM} are the bulk ground state energies of the AFM area (C-AFM-I) and FM area, respectively. The factor $1/2$ accounts for the two interfaces per supercell. When calculating the energies of AFM and FM LSMO, the same supercell is used to avoid possible numerical artifacts, and

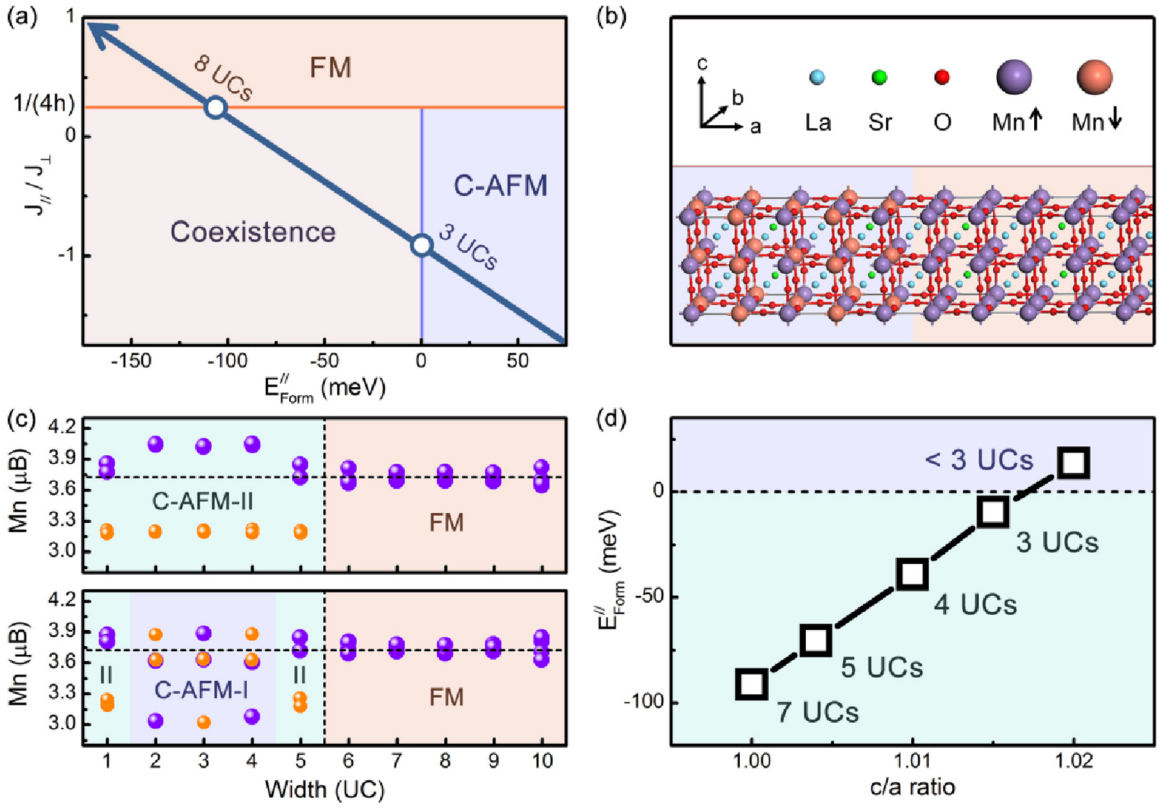

FIG. 7. (a) Phase diagram of LSMO films as a function of $E^{\parallel}_{\mathrm{Form}}$ and $J_{\parallel}/J_{\perp}$. (b) Structure of the C-AFM/FM supercell. The blue and yellow areas represent C-AFM and FM regions, respectively. (c) The absolute values of Mn magnetic moments in each Mn-O_2 plane. The violet and yellow balls represent spin-up and spin-down, respectively. (d) The dependence of the in-plane formation energy on the *c*/*a* ratio.

a dense Monkhorst-Pack k point of $2 \times 6 \times 6$ was used in all calculations. Surprisingly, the interfacial layer in the AFM side tends to adopt the AFM-II phase even when the AFM-I phase is assumed in calculations. Furthermore, the lowest energy configuration prefers to have the C-AFM-II phase in the entire AFM region as shown in the top panel in Fig. 7(c). With this magnetic alignment, the calculated $E^{\parallel}_{\mathrm{Form}}$ is -76 meV. If we force the AFM-I phase in the AFM region as depicted in the bottom panel in Fig. 7(c), $E^{\parallel}_{\mathrm{Form}}$ is only -5 meV. We may perceive that the FM disks are surrounded by a few metallic AFM-II layers in the AFM-I matrix. In addition, $E^{\parallel}_{\mathrm{Form}}$ strongly depends on the change of the c/a ratio of the LSMO film, as shown in Fig. 7(d), and $E^{\parallel}_{\mathrm{Form}}$ is positive for $c/a > 1.015$. This explains why only the AFM-I phase is observed when film is thinner than 3UCs as the *c*/*a* ratio is large. These results indicate the importance of the subtle interplay between lattice strain and COO phase transition for the formation of magnetic nanostructures in complex magnetic oxides.

As shown in Fig. 5(b), the insulator to metal transition occurs at 8 UCs, where the shear strain relieves abruptly and the films turn into a uniform FM metallic system. Figure 2(b) indicates that the unusual expansion in all *a*, *b*, and *c* axes for LSMO films thinner than 7 UCs disappears at 8 UCs. The *c*-axis expansion has been understood as a consequence of the strong interface effect that favors occupying the Mn $d_{3z^2-r^2}$ orbital and the C-type AFM alignment [14,15,21,37,38]. This tendency is further reinforced by some Sr segregation [39]. Figure 8 shows our aberration-corrected high angle annular dark field scanning transmission electron microscopy (HAADF-STEM) and energy-dispersive x-ray spectroscopy (EDXS) results on the LSMO/STO (001) interface, and it indicates that the Sr segregation indeed occurs within 1–3 unit cells (see Appendix F). However, it should be noted that the Sr segregation cannot be the main reason for stabilizing the C-type AFM state of the interfacial LSMO layers, since the entire film turns back into a uniform FM state above 8 UCs. By increasing the thickness (>3 UCs), the influence of the interface on the top LSMO layers decreases. The *c*-axis expansion becomes energetically less favorable in the tensile strained condition, and the *c*/*a* ratio gradually decreases. At 8 UCs, the shear strain relief abruptly occurs by forming twinning domains along the [100] and [010] directions with a periodicity of two atomic lattice spacing. Such a dramatic structural change reduces both shear strain energy and extra energy cost for lattice expansion in all three directions. This energy cost does not exist in compressively strained systems since the *c*-axis expansion is energetically favored, explaining why the LSMO thin films on substrates like $LaAlO_3$ have a higher critical thickness for the AFM to FM phase transition [14,40–42]. The thick LSMO films restore the rhombohedral symmetry and become a uniform FM metallic system as the LSMO bulk. Therefore, the shear strain plays a key role to force the LSMO films to form the peculiar magnetic

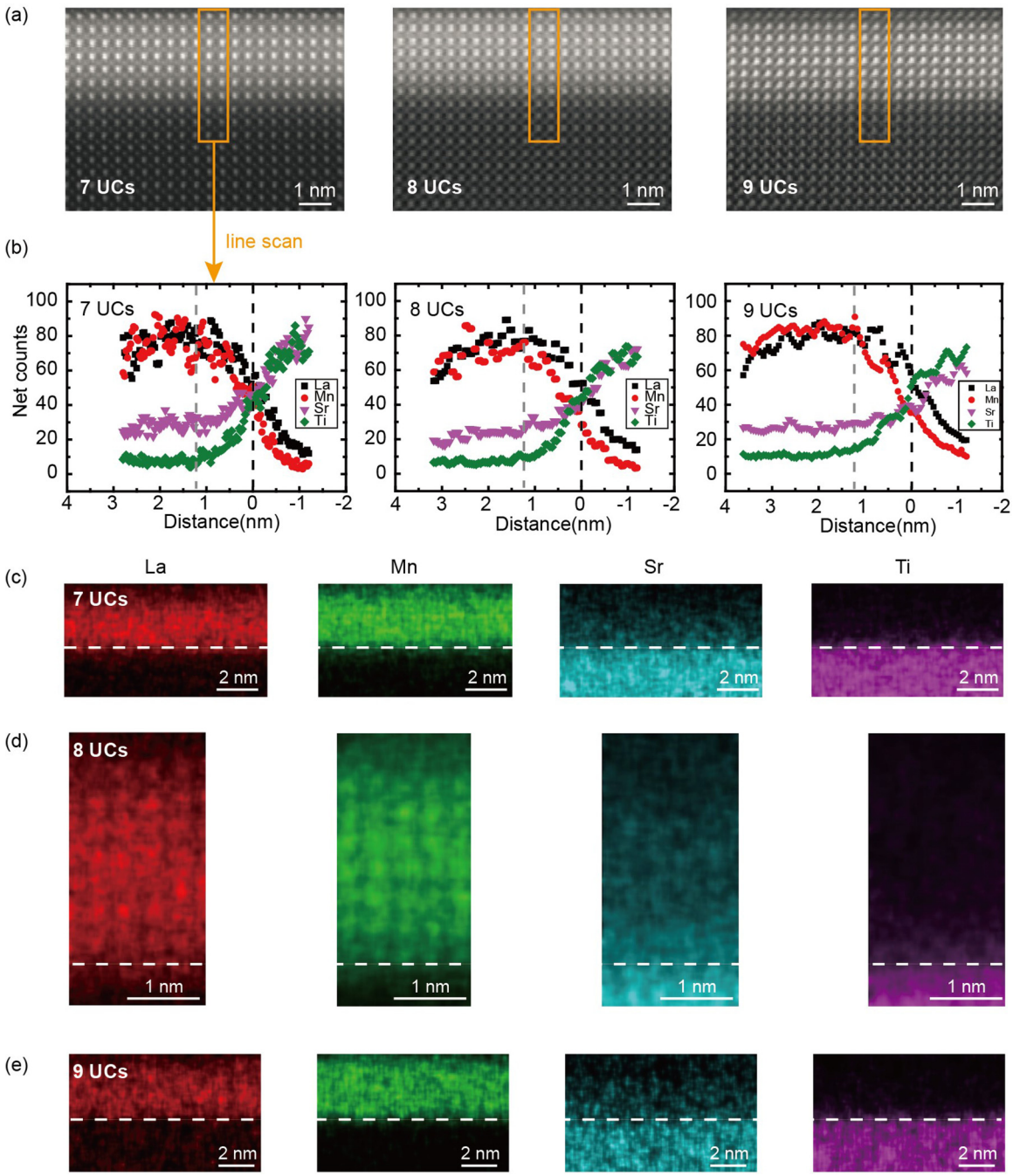

FIG. 8. Determination of atomic scale structure and chemistry of LSMO/STO ultrathin films. (a) The high angle annular dark field scanning transmission electron microscopy image of 7–9-UC LSMO/STO thin films. (b) EDX results for La *L*, Mn *K*, Sr *L*, and Ti *K* shells taken from the area across LSMO/STO interface. The black dashed lines indicate the position of the interface, and the gray dashed lines indicate the position of 3 UCs, so the Sr diffusion range of these films is within 3 UCs. (c)–(e) High resolution EDX elemental mapping images for [001] direction in 7–9-UC LSMO/STO films for the La *L*, Mn *K*, Sr *L*, and Ti *K* shells, respectively. The white dashed lines indicate the position of the interface.

phase depicted in Fig. 5(a), as also suggested by the DFT calculations.

IV. SUMMARY

In summary, we have observed an unusual electronic and magnetic phase separation phenomenon in LSMO ultrathin films grown on STO. Our experimental measurements indicate that the 3 base UCs of 4–7-UC LSMO films retain the AFM phase, while the additional LSMO UCs show an insulating and blocked superparamagnetic behavior with a low net magnetization. We explain the observation with the formation of the inhomogeneous phase in the additional unit cells, consisting of FM nanodisks in the AFM matrix. Our first principles calculations show that the phase separation is caused by a rather counterintuitive mechanism, i.e., the

formation of FM/AFM boundaries release rather than cost energy. After this narrow thickness range, the shear strain is suddenly relieved at 8 UCs, and the LSMO films adopt the homogeneous bulk-like ferromagnetic metallic state. Our studies indicate the importance of the interplay between strain, charge, orbital, and spin orderings in complex systems. The integration and control of these degrees of freedom can be useful for the design of storage and operation units for quantum information technologies.

ACKNOWLEDGMENTS

We thank C. S. Tian, Y. Xu, Y. Z. Wu, and L. Sun for helpful discussions. This work was supported by the National Key Research and Development Program of China (2016YFA0300701, 2016YFA0300702, and 2015CB921400), Shanghai Municipal Natural Science Foundation (18JC1411400, 18ZR1403200), and the Program of Shanghai Academic Research Leader (18XD1400600, 17XD1400400). The authors thank Beamline BL14B1 (Shanghai Synchrotron Radiation Facility) for providing the beam time and help during experiments. This work made use of the resources of the Ernst Ruska-Centre for Microscopy and Spectroscopy with Electrons in Forschungszentrum Jülich and the National Centre for Electron Microscopy in Beijing. The authors thank M. Kruth, L. Jin, J. Mayer, and R. Dunin-Borkowski for helpful assistance. Z.C.W. and X.Y.Z. are grateful for the support of the National Key Research and Development Program (2016YFB0700402) and the Scholarship of Strategic Partnership RWTH-Aachen University and Tsinghua University.

APPENDIX A: SAMPLE PREPARATION PROCEDURE AND DETERMINATION OF THE ABSOLUTE MAGNETIC MOMENT

The post-anneal procedure is really important for the growth of manganite films. At the beginning of sample growth, we carefully compared the difference between different oxygen environments, growth temperature, and post-anneal time. Our data shows that when we set growth temperature at about 820 °C and the oxygen environment of 3×10^{-2} Torr, the post-anneal procedure seems not to change the magnetic properties of the films. Figures 9(a) and 9(b) shows the comparison of 30-UC thick uniform LSMO films accompanied by *in situ* 2 min (red line) and 30 min (black line) post-anneal time after the growth of each unit cell. It seems that the post-anneal procedure does not change the

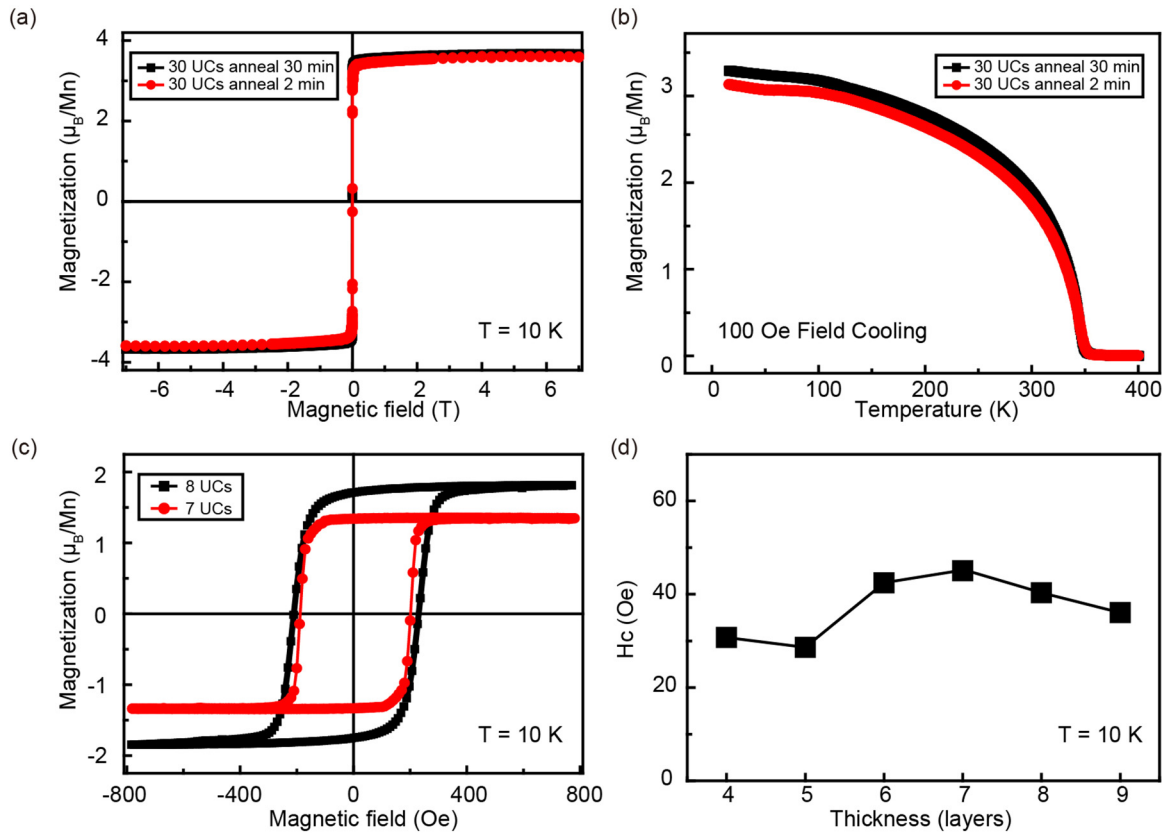

FIG. 9. Magnetic property of different thicknesses of LSMO films. (a) The magnetic hysteresis loops of two 30-UC thick LSMO films with different annealing procedure measured at 10 K by SQUID. The black (red) line represent the film with annealing time of 30 [Eq. (2)] min after the growth of every unit cell layer. The magnetic field applied in the easy axis, i.e., [110] direction, and they both show the saturation moment of 3.6 μ_B/Mn. (b) Temperature dependence magnetization of LSMO films with different annealing procedure [corresponds to Fig. 9(a)], measured field cooling in an external field of 100 Oe applied in the in-plane [110] direction. (c) The magnetic hysteresis loops of 7- and 8-UC-thick LSMO films measured at 10 K, which show the saturation moment of 1.3 and 1.8 μ_B/Mn, respectively. (d) Thickness dependence of coercive field (H_c) of LSMO films plotted according to Fig. 3(a).

magnetic moment (the absolute value of the magnetic moment is determined to be $\sim 3.6\,\mu_B$/Mn, close to that of the bulk $\sim 3.7\,\mu_B$/Mn [11]), not the Curie temperature ($\sim$355 K). Note that a linear background signal from the STO substrate has been subtracted from the raw data. It is reasonable since the oxygen pressure we used is high enough to satisfy the growth that it does not need to anneal more to enhance the magnetization. After the confirmation, we have prepared three kinds of different LSMO/STO films. Type I: a uniform film with specific thickness grown on Nb-doped STO, e.g., 7 UCs and 8 UCs, to satisfy the STM measurement. Type II: a wedge sample grown on Nb-doped STO (still use Nb-doped STO to minimize the difference between different substrates). Type III: other uniform films with specific thickness. For the type I sample, to ensure an atomically flat surface, the films were *in situ* annealed for 30 min after the growth of each unit cell layer except the last layer to avoid the surface reconstruction [43]. For the type II wedge sample, the films were *in situ* annealed for about 2 min after the growth of each unit cell unavoidably, since it needs time to carry on the shutter procedure. The use of the shutter procedure will introduce a systematic difference in the post-treatment of different parts of the sample, which may induce some arguments. Here, we would like to introduce the further detailed growth procedure and the comparison we have made after measurement. When we grow the wedge sample, we place a shutter between the PLD plume and STO substrate, very close the substrate to shade it. After the RHEED signal shows that one layer's growth is finished, we stop the plume first then move the sample stage into the shade in some area (0.6-mm width) of the substrate into the back of shutter, and then grow another unit cell again. So it seems that the first films experience more anneal time. Although we have checked that the post-anneal time does not change the magnetic properties above, it is to better rule out the influence of this issue. After finishing the MOKE measurement, we anneal the wedge sample in the chamber with oxygen again, than measure it once more. It seems that post-anneal does not change the magnetic properties of wedge sample either. Finally, for the type III sample, the films were *in situ* annealed for about 2 min after the growth of each unit cell to keep the same growth condition, and the films used to measure the resistance were grown on insulating STO (only these two samples are grown on insulating STO, Fig. 11), others are still grown on Nb-doped STO.

To enhance the reliability of MOKE results, we also measure the magnetization of 7- and 8-UC- thick LSMO films by SQUID. Figure 9(c) shows the typical hysteresis curve of 7- and 8-UC LSMO films with the magnetic field applied in the easy axis, i.e., the [110] direction. The absolute value of the magnetic moment is determined to be $1.3\,\mu_B$/Mn of the 7-UC film if considering all of the manganese atoms, and $2.2\,\mu_B$/Mn if only considering the layers above the first three unit cells antiferromagnetic base layers (it means 4/7 manganese atoms count). The estimated magnetic moment of 7-UC films measured by MOKE is about $1.8\,\mu_B$/Mn (see the main text). There is about 10% deviation between MOKE estimation and SQUID measurement. We infer that the deviation may result from two factors. The first is that the signals from STO substrates show different responses to two different experiment techniques (MOKE and SQUID), which may introduce some impact on not such a big magnetic signal. The second is that the estimated magnetic moment of the 7-UC film measured by MOKE is calculated from the value of 30-UC LSMO films (including a one-time calculation of the film area), and the absolute magnetic moment of 7-UC film measured by SQUID is calculated directly (including a second calculation of the film area), so the deviation may induced by these conversions. As for the 8-UC LSMO film, the absolute value of the magnetic moment is determined to be $\sim 1.8\,\mu_B$/Mn considering all of the manganese atoms. It is obvious that the film is in a mixed phase state since the absolute value of saturation magnetization is smaller than bulk. However, the exact magnetic structure of this film (regime III) remains unknown. It seems that the first three AFM base layers at the interface have been changed, but we do not know to what extent.

Figure 9(d) shows the thickness dependence of the coercive fields of LSMO films measured by MOKE extracted from Fig. 3(a). It seems that the coercive field of 4–7-UC- thick films have no obvious trend. We infer that it may be attributed to the unconventional magnetic properties of the ultrathin films. When we talk about the conventional pure (uniform) ferromagnetic films, the coercive field of films may increase with decreasing thickness intuitively. However, as mentioned in the main text, the 4–7-UC-thick LSMO/STO films are in a mixed phase state and nonuniform in both vertical and lateral directions. So it might be different from the conventional ferromagnetic films and show a more complicated state of this bad parameter that may depend on almost everything.

APPENDIX B: XRD MEASUREMENTS OF THE THICKNESS WEDGE SAMPLE

The error bars of Fig. 2(b) are obtained from the combination of growth and measurement procedures. First, we would like to discuss the accuracy of thickness. As mentioned in the main text, the thickness of LSMO films was monitored by unit cell intensity oscillations of RHEED. So the thickness is almost accurate. More precisely, as shown in Figs. 1(a) and 1(b), although there might be some patches and holes on the film surfaces, the statistical deviation of thickness is less than 0.1 UC. For Fig. 1(a), the estimated statistic deviation is $(-)$ 0.08 UC, and for Fig. 1(b), it is about $(+)$ 0.05 UC. So the deviation of thickness can be estimated about 0.1 UC. Second, we discuss the accuracy of the thickness measurement: (1) Growth condition: the designed width of the layer step increased layer by layer is about 0.6 mm. When we carefully control the shielded area, the movement accuracy of our movable sample stage in the PLD chamber is 0.01 mm, so there might be 0.01-mm errors. (2) The beam size at the sample is approximately $0.2 \times 0.2\,\text{mm}^2$, which is about one third of the width of designed layer step in the movement direction. The movement accuracy of the XRD measurement is about 0.001 mm, far smaller than the beam size. So the deviation of thickness measurement is negligible since the growth condition accuracy (0.01 mm) is far smaller than the designed width (0.6 mm) and beam width (0.2 mm). Meanwhile, the movement accuracy (0.001 mm) is far smaller than beam width (0.2 mm). Therefore, the error bars in Fig. 2(b) calculated from the deviation of thickness are estimated to be

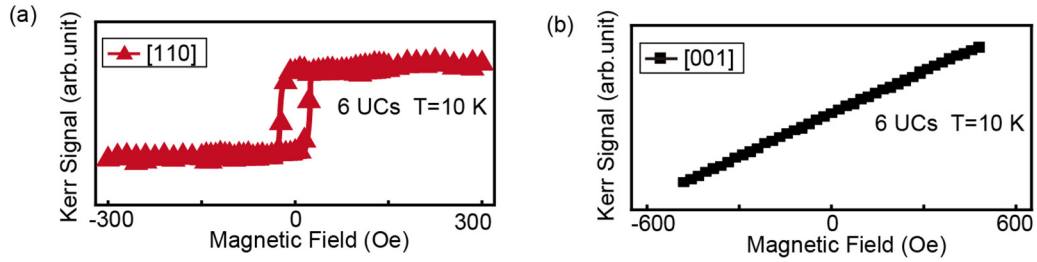

FIG. 10. (a) Typical MOKE hysteresis loops of the 6-UC LSMO film measured at 10 K, with magnetic field applied along in-plane [110] easy magnetization axis. (b) Polar-MOKE measurement on the 6-UC LSMO film with magnetic field applied along surface normal.

0.1 UC. More detailed information about beamline BL14B1 can be found in Ref. [44].

APPENDIX C: MOKE MEASUREMENTS OF THE LSMO THICKNESS WEDGE SAMPLE

The thickness-dependent Kerr intensity (proportional to magnetization in the thin film regime [45]) is measured by MOKE from the thickness wedge sample. The experimental setup and the schematic of the LSMO wedge sample are shown in Fig. 2(a). Since the wedge sample consists of films with different thicknesses grown under the same conditions, we can obtain a reliable comparison of the magnetic properties of the LSMO ultrathin films with different thickness. Figure 10(a) shows the typical MOKE hysteresis loops of the 6-UC LSMO film measured at 10 K, with the magnetic field applied along the in-plane [110] direction. Figure 10(b) shows that there is no magnetic hysteresis loop with the field ($\sim$ 500 Oe) applied along the out-of-plane [001] direction, indicating that the easy magnetization axis of the LSMO ultrathin films is in the film plane. The in-plane easy magnetization axis is determined to be in the [110] direction (see initial magnetization curves measured along different directions shown in Fig. 6). Note that the linear background signal from the STO substrate has been subtracted from the raw data. The saturation magnetization, Ms, indicated in Fig. 3(b) of the main text, is determined from the measured MOKE hysteresis loops by $Ms = A*\frac{(\mathrm{Kerr}^{+}-\mathrm{Kerr}^{-})}{2}$. The prefactor A can be regarded as a constant when measuring films with different thicknesses in one wedge sample with our experimental setup [45]. $\mathrm{Kerr}^{+/-}$ denote the saturation Kerr signals.

APPENDIX D: TRANSPORT PROPERTIES MEASUREMENT

The temperature-dependent resistance under the zero magnetic field for ultrathin LSMO films of 7 and 8 UCs are acquired using Physical Properties Measurement System (PPMS), as shown in Fig. 11. The 8-UC film shows a metallic behavior, while the 7-UC film is insulating over the whole temperature range.

APPENDIX E: CALCULATION OF THE SIZE OF THE SUPERPARAMAGNETIC NANODISKS IN THE 6-UC FILM

When a strong enough external magnetic field is applied to a superparamagnetic system, it will align the magnetization of the nanoparticles along the field direction by overcoming the anisotropy energy. Once the magnetic field is removed, the magnetization will decay with time due to the thermal fluctuation. At finite temperatures, there is a finite probability for the magnetization of the nanoparticles to flip and reverse its direction. And it can be described by the Néel-Arrhenius equation [30]:

$$\tau = \tau_0 \exp\left(\frac{KV}{K_B T}\right), \tag{E1}$$

where τ is the Néel relaxation time, τ_0 is a relaxation-time constant that is typically around $10^{-9} - 10^{-10}$ s [31]. K is the anisotropy constant and V is the volume of the nanoparticles. In addition, Néel also proposed that the decay of the magnetization of the nanoparticles can be approximately described as

$$M_r(t) = M_i \exp\left(-\frac{t}{\tau}\right), \tag{E2}$$

where M_i is the initial magnetization and M_r is the remanent magnetization after switching off the magnetic field. To obtain the decay time directly by experiments, we plot the relaxation behavior as ln-*linear* scale according to Eq. (2), which shows that $\ln(M_r(t))$ is proportional to time (t), and then the slope corresponds to $-\frac{1}{\tau}$. In this way, we can obtain the decay time (τ) directly by fitting the experimental data using Eq. (2).

Figures 12(a) and 12(b) show the fitting of the time-dependent decay behavior of the 6-UC LSMO film at 77 and 79 K, respectively. The best fit yields $\tau_1 = 19.5$ s (at 77 K)

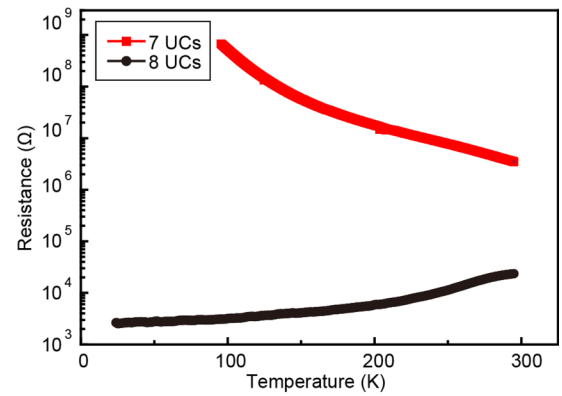

FIG. 11. The temperature-dependent resistance of 7- and 8-UC LSMO films are measured under zero magnetic field using PPMS. A clear insulator to metal transition occurs between 7 and 8 UCs.

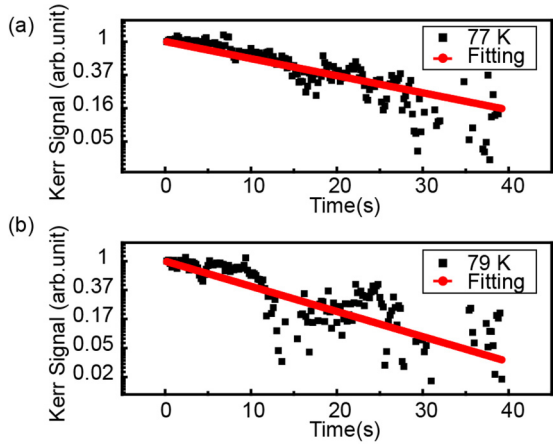

FIG. 12. Determination of the size of superparamagnetic nanodisks. (a) and (b) are fitting of the decay behavior of the remanent magnetization at 77 and 79 K by plotting the experiment data in ln-*linear* scale according to Eq. (2), respectively. Red dots: fittings; black dots: experimental data.

and $\tau_2 = 10.5$ s (at 79 K). According to Eq. (1), assuming that τ_0 values at these two temperatures are the same, we have

$$\frac{\tau_1}{\tau_2} = \exp\left(\frac{KV}{K_B T_1} - \frac{KV}{K_B T_2}\right)$$

or

$$KV = \ln\frac{\tau_1}{\tau_2} * K_B * \frac{T_2 * T_1}{T_2 - T_1}. \tag{E3}$$

Here $T_1 = 77$ K and $T_2 = 79$ K. For the 6-UC LSMO ultrathin film, it has been shown in Fig. 10(b) that the hard axis is along the surface normal. Here, we measure both the effective out-of-plane magnetic anisotropy constant $K_\perp$ and effective in-plane magnetic anisotropy $K_\parallel$ by SQUID using the initial magnetization curves at 77 K, which are shown in Fig. 6. Since the effective magnetic anisotropy constant K can be obtained using formula $K = Hs \times Ms/2$ [46]. It is clear that $K_\parallel$ is far smaller than $K_\perp$, as the corresponding $Hs_\parallel$ is about one order of magnitude smaller that $Hs_\perp$. So it is easier for spins to overcome the in-plane anisotropy barrier rather than the out-of-plane anisotropy barrier. Figure 6 shows the initial magnetization curves of the 6-UC LSMO ultrathin film along different in-plane directions, from which we obtain $Hs_\parallel \sim 2000$ Oe and $Ms \sim 1.8\,\mu_B$/Mn, yielding $K \sim 2 \times 10^3$ J/m^3. The average volume of the ferromagnetic nanoparticles is obtained to be $V \sim 13\,000$ nm^3 from Eq. (3). This in turn gives the attempt time $\tau_0 \sim 4.6 \times 10^{-10}$ s, a reasonable value for a superparamagnetic system [31]. Considering the fact that the ferromagnetic nanoparticles have a disk shape of 3-UC in height (1.2 nm), the nanodisks are roughly 120 nm in average diameter.

APPENDIX F: ATOMIC STRUCTURAL AND CHEMICAL INFORMATION OF THE LSMO/STO(001) INTERFACE REVEALED BY STEM

HAADF STEM imaging [47] was carried out in a FEI Titan G2 80–200 CREWLEY "ChemiSTEM" microscope. It is a fourth generation transmission electron microscope that has been specifically designed for the investigation of a wide range of solid state phenomena taking place on the atomic scale of both the structure and chemical composition [48]. The electron microscopy is equipped with a high-brightness field emission gun (X-FEG), a monochromator unit, a probe spherical aberration (Cs) corrector, and a super-X EDXS system. The attainable spatial resolution of the microscope is 78 pm. EDXS mapping with atomic resolution was performed to determine the elemental distribution of La, Sr, Mn, Ti, and O also on the ChemiSTEM microscope equipped with a super-X EDXS system. The attainable energy resolution of the EDX detector is < 136 eV @ Mn $K\alpha$. A higher beam current of 280 pA was used with a longer dwell time of 0.1 msec per pixel repeated 200 times. Spatial drift was corrected with a simultaneous image collector. La L edge, Sr K edge, Mn K edge, Ti K edge, and O K edge were used for elemental mapping of these species. All of the microscopes were operated at 200 kV. The convergence semiangle for STEM imaging was approximately 22 mrad, while the collection semiangle was 70–176 or 200 mrad and a probe current of 100 pA for HAADF imaging.

To characterize the structural and chemical information of the LSMO/STO interface, we performed high-resolution STEM on three LSMO ultrathin films with 7-, 8-, and 9-UC thickness, which have the magnetic states in region II (7 UCs), region III (8 UCs), and region IV (9 UCs), respectively [see Fig. 3(b) in main text]. As shown by the HAADF-STEM image in Fig. 8(a), the epitaxial growth of the LSMO ultrathin films on the STO (001) substrates are of high quality. The distribution of the chemical components of the LSMO/STO films is analyzed using EDXS, as shown in Fig. 8(b). The net counts are obtained from the peak of La L, Mn K, Sr L and Ti K shells. The interface is marked by the vertical black dashed line and the gray dashed line are guides to the eyes to identify the Sr diffusion length. It can be seen from the figures that the Sr segregation from the STO substrate to the LSMO films occurs only within 1–3 UCs at the interface. In addition, there is no detectable surface Sr segregation in our TEM experiments. Figures 8(c)–8(e) show the high resolution EDXS elemental mapping images for the [001] direction in LSMO/STO films for the La L, Mn K, Sr L, and Ti K shells. The real space data also confirms that the Sr diffusion is near the interface.

[1] K. J. Lai, M. Nakamura, W. Kundhikanjana, M. Kawasaki, Y. Tokura, M. A. Kelly, and Z. X. Shen, Science **329**, 190 (2010).
[2] J. Shao, H. Liu, K. Zhang, Y. Yu, W. C. Yu, H. X. Lin, J. B. Niu, K. Du, Y. F. Kou, W. G. Wei, F. L. Lan, Y. Y. Zhu, W. B. Wang, J. Xiao, L. F. Yin, E. W. Plummer, and J. Shen, Proc. Natl. Acad. Sci. USA **113**, 9228 (2016).
[3] P. Beaud, A. Caviezel, S. O. Mariager, L. Rettig, G. Ingold, C. Dornes, S-W. Huang, J. A. Johnson, M. Radovic, T. Huber,

T. Kubacka, A. Ferrer, H. T. Lemke, M. Chollet, D. Zhu, J. M. Glownia, M. Sikorski, A. Robert, H. Wadati, M. Nakamura, M. Kawasaki, Y. Tokura, S. L. Johnson, and U. Staub, Nature Mater. **13**, 923 (2014).

[4] S. Jin, T. H. Tiefel, M. McCormack, R. A. Fastnacht, R. Ramesh, and L. H. Chen, Science **264**, 413 (1994).

[5] J. H. Park, E. Vescovo, H. J. Kim, C. Kwon, R. Ramesh, and T. Venkatesan, Nature (London) **392**, 794 (1998).

[6] S. Mathews, R. Ramesh, T. Venkatesan, and J. Benedetto, Science **276**, 238 (1997).

[7] Z. H. Xiong, D. Wu, Z. V. Vardeny, and J. Shi, Nature (London) **427**, 821 (2004).

[8] L. E. Hueso, J. M. Pruneda, V. Ferrari, G. Burnell, J. P. Valdés-Herrera, B. D. Simons, P. B. Littlewood, E. Artacho, A. Fert, and N. D. Mathur, Nature (London) **445**, 410 (2007).

[9] D. L. Sun, L. F. Yin, C. J. Sun, H. W. Guo, Z. Gai, X. G. Zhang, T. Z. Ward, Z. H. Cheng, and J. Shen, Phys. Rev. Lett. **104**, 236602 (2010).

[10] A. Chanthbouala, A. Crassous, V. Garci, K. Bouzehouane, S. Fusil, X. Moya, J. Allibe, B. Dlubak, J. Grollier, S. Xavier, C. Deranlot, A. Moshar, R. Proksch, N. D. Mathur, M. Bibes, and A. Barthélémy, Nat. Nanotechnol. **7**, 101 (2011).

[11] A. Urushibara, Y. Moritomo, T. Arima, A. Asamitsu, G. Kido, and Y. Tokura, Phys. Rev. B **51**, 14103 (1995).

[12] B. Nadgorny, I. I. Mazin, M. Osofsky, R. J. Soulen, Jr., P. Broussard, R. M. Stroud, D. J. Singh, V. G. Harris, A. Arsenov, and Ya. Mukovskii, Phys. Rev. B **63**, 184433 (2001).

[13] M. Huijben, L. W. Martin, Y. H. Chu, M. B. Holcomb, P. Yu, G. Rijnders, D. H. A. Blank, and R. Ramesh, Phys. Rev. B **78**, 094413 (2008).

[14] A. Tebano, C. Aruta, S. Sanna, P. G. Medaglia, G. Balestrino, A. A. Sidorenko, R. De Renzi, G. Ghiringhelli, L. Braicovich, V. Bisogni, and N. B. Brookes, Phys. Rev. Lett. **100**, 137401 (2008).

[15] C. Aruta, G. Ghiringhelli, V. Bisogni, L. Braicovich, N. B. Brookes, A. Tebano, and G. Balestrino, Phys. Rev. B **80**, 014431 (2009).

[16] B. Kim, D. Kwon, J. H. Song, Y. Hikita, B. G. Kim, and H. Y. Hwang, Solid. State. Commun. **150**, 598 (2010).

[17] M. B. Lepetit, B. Mercey, and C. Simon, Phys. Rev. Lett. **108**, 087202 (2012).

[18] Y. J. Shi, Y. Zhou, H. F. Ding, F. M. Zhang, L. Pi, Y. H. Zhang, and D. Wu, Appl. Phys. Lett. **101**, 122409 (2012).

[19] Z. L. Liao, F. M. Li, P. Gao, L. Li, J. D. Guo, X. Q. Pan, R. Jin, E. W. Plummer, and J. D. Zhang, Phys. Rev. B **92**, 125123 (2015).

[20] Å. Monsen, J. E. Boschker, F. Macià, J. W. Wells, P. Nordblad, A. D. Kent, R. Mathieu, T. Tybell, and E. Wahlström, J. Magn. Magn. Mater. **369**, 197 (2014).

[21] A. Tebano, A. Orsini, P. G. Medaglia, D. Di Castro, G. Balestrino, B. Freelon, A. Bostwick, Young Jun Chang, G. Gaines, E. Rotenberg, and N. L. Saini, Phys. Rev. B **82**, 214407 (2010).

[22] M. Kawasaki, K. Takahashi, T. Maeda, R. Tsuchiya, M. Shinohara, O. Ishiyama, T. Yonezawa, M. Yoshimoto, and H. Koinuma, Science **266**, 1540 (1994).

[23] U. Gebhardt, N. V. Kasper, A. Vigliante, P. Wochner, H. Dosch, F. S. Razavi, and H. U. Habermeier, Phys. Rev. Lett. **98**, 096101 (2007).

[24] S. W. Jin, G. Y. Gao, Z. Huang, Z. Z. Yin, X. Zheng, and W. B. Wu, Appl. Phys. Lett. **92**, 261901 (2008).

[25] O. I. Lebedev, G. V. Tendeloo, S. Amelinckx, F. Razavi, and H. U. Habermeier, Philos. Mag. A. **81**, 797 (2001).

[26] J. L. Maurice, F. Pailloux, A. Barthélémy, O. Durand, D. Imhoff, R. Lyonnet, A. Rocher, and J. P. Contour, Philos. Mag. **83**, 3201 (2003).

[27] A. Vailionis, H. Boschker, W. Siemons, E. P. Houwman, D. H. A. Blank, G. Rijnders, and G. Koster, Phys. Rev. B **83**, 064101 (2011).

[28] S. K. Streiffer, C. B. Parker, A. E. Romanov, M. J. Lefevre, L. Zhao, J. S. Speck, W. Pompe, C. M. Foster, and G. R. Bai, J. Appl. Phys. **83**, 2742 (1998).

[29] L. Lutterott, D. Chateigner, S. Ferrari, and J. Ricote, Thin Solid Films, **450**, 34 (2004).

[30] L. Néel, Ann. Geophys. **5**, 99 (1949).

[31] A. Aharoni, *Introduction to the Theory of Ferromagnetism* (Oxford University Press, New York, 1996).

[32] G. Kresse and J. Furthmüller, Phys. Rev. B **54**, 11169 (1996).

[33] G. Kresse and J. Furthmüller, Comput. Mater. Sci. **6**, 15 (1996).

[34] P. E. Blöchl, Phys. Rev. B **50**, 17953 (1994).

[35] G. Kresse and D. Joubert, Phys. Rev. B **59**, 1758 (1999).

[36] J. P. Perdew, K. Burke, and M. Ernzerhof, Phys. Rev. Lett. **77**, 3865 (1996).

[37] A. Tebano, C. Aruta, P. G. Medaglia, F. Tozzi, G. Balestrino, A. A. Sidorenko, G. Allodi, R. De Renzi, G. Ghiringhelli, C. Dallera, L. Braicovich, and N. B. Brookes, Phys. Rev. B **74**, 245116 (2006).

[38] Y. Tokura and N. Nagaosa, Science **288**, 462 (2000).

[39] R. Herger, P. R. Willmott, C. M. Schlepütz, M. Björck, S. A. Pauli, D. Martoccia, B. D. Patterson, D. Kumah, R. Clarke, Y. Yacoby, and M. Döbeli, Phys. Rev. B **77**, 085401 (2008).

[40] A. Tebano, A. Orsini, D. Di Castro, P. G. Medaglia, and G. Balestrino, Appl. Phys. Lett. **96**, 092505 (2010).

[41] S. I. Khartsev, P. Johnsson, and A. M. Grishin, J. Appl. Phys. **87**, 2394 (2000).

[42] M. Angeloni, G. Balestrino, N. G. Boggio, P. G. Medaglia, P. Orgiani, and A. Tebano, J. Appl. Phys. **96**, 6387 (2004).

[43] K. Fuchigami, Z. Gai, T. Z. Ward, L. F. Yin, P. C. Snijders, E. W. Plummer, and J. Shen, Phys. Rev. Lett. **102**, 066104 (2009).

[44] T. Y. Yang, W. Wen, G. Z. Yin, X. L. Li, M. Gao, Y. L. Gu, L. Li, Y. Liu, H. Lin, X. M. Zhang, B. Zhao, T. K. Liu, Y. G. Yang, Z. Li, X. T. Zhou, and X. Y. Gao, Nucl. Sci. Tech. **26**, 021001 (2015).

[45] Z. Q. Qiu and S. D. Bader, Rev. Sci. Instrum. **71**, 1243 (2000).

[46] B. D. Cullity, *Introduction to Magnetic Materials* (Addison-Wesley, Reading, 1972).

[47] D. E. Jesson and S. J. Pennycook, Proc. R. Soc. Lond. A. **449**, 273 (1995).

[48] A. Kovács, R. Schierholz, and K. Tillmann, JLSRF **2**, A43 (2016).